



NRC Publications Archive Archives des publications du CNRC

In situ formation of aluminide intermetallic particles in a AM60B alloy Ye, Hai Zhi; Liu, Xing Yang

This publication could be one of several versions: author's original, accepted manuscript or the publisher's version. /
La version de cette publication peut être l'une des suivantes : la version prépublication de l'auteur, la version
acceptée du manuscrit ou la version de l'éditeur.
For the publisher's version, please access the DOI link below. / Pour consulter la version de l'éditeur, utilisez le lien
DOI ci-dessous.

Publisher's version / Version de l'éditeur:

<https://doi.org/10.1016/j.msea.2006.03.062>

Materials Science and Engineering: A, 427, pp. 27-34, 2006

NRC Publications Record / Notice d'Archives des publications de CNRC:

<https://nrc-publications.canada.ca/eng/view/object/?id=dc30425b-6a8c-49fa-b183-65af8efd76a7>

<https://publications-cnrc.canada.ca/fra/voir/objet/?id=dc30425b-6a8c-49fa-b183-65af8efd76a7>

Access and use of this website and the material on it are subject to the Terms and Conditions set forth at

<https://nrc-publications.canada.ca/eng/copyright>

READ THESE TERMS AND CONDITIONS CAREFULLY BEFORE USING THIS WEBSITE.

L'accès à ce site Web et l'utilisation de son contenu sont assujettis aux conditions présentées dans le site

<https://publications-cnrc.canada.ca/fra/droits>

LISEZ CES CONDITIONS ATTENTIVEMENT AVANT D'UTILISER CE SITE WEB.

Questions? Contact the NRC Publications Archive team at

PublicationsArchive-ArchivesPublications@nrc-cnrc.gc.ca. If you wish to email the authors directly, please see the
first page of the publication for their contact information.

Vous avez des questions? Nous pouvons vous aider. Pour communiquer directement avec un auteur, consultez la
première page de la revue dans laquelle son article a été publié afin de trouver ses coordonnées. Si vous n'arrivez
pas à les repérer, communiquez avec nous à PublicationsArchive-ArchivesPublications@nrc-cnrc.gc.ca.



National Research
Council Canada

Conseil national de
recherches Canada

Canada

In-situ formation of aluminide intermetallic particles in AM60B alloy

Hai Zhi Ye and Xing Yang Liu*

Integrated Manufacturing Technologies Institute, National Research Council of Canada,
London, ON, Canada N6G 4X8

*. Corresponding author: Tel: 1-519-430-7042, Fax: 1-519-430-7064, Email:

xingyang.liu@nrc.gc.ca.

Abstract

Adding nickel to an AM60B magnesium alloy during melting produced two types of intermetallic particles in the alloy: manganese nickel aluminide ($\text{Al}_{60}\text{Mn}_{11}\text{Ni}_4$) and nickel aluminide ($\text{Al}_{0.42}\text{Ni}_{0.58}$). $\text{Al}_{60}\text{Mn}_{11}\text{Ni}_4$ particles were normally fine and uniformly distributed in the cast ingot, resulting in grain refinement and significant improvement of tensile properties. $\text{Al}_{0.42}\text{Ni}_{0.58}$ particles are formed when nickel is added in powder form, and prone to coarsening and segregation during the melting process.

Key words: aluminide particles, in-situ formation, magnesium alloy, grain refinement, tensile properties

1. Introduction

Magnesium is an attractive engineering material for the transportation industry because of its high specific strength, good damping capacity, excellent castability, and superior machinability. The relatively poor high-temperature strength of commercial magnesium alloys, however, limits their applications to components working at relatively low

temperatures. The most widely used commercial magnesium alloys, such as AM60B and AZ91, for example, can only be used at temperatures up to 120 °C, due to the relatively low thermal stability of $Mg_{17}Al_{12}$ [1], the main strengthening phase in the Mg-Al alloy systems.

Developing magnesium composites by reinforcing the matrix with phases that are thermally stable has been widely explored for improving the high-temperature mechanical properties. Both ceramics (such as SiC [2] and Al_2O_3 [3]) and elemental metals (such as Ni [4] and Cu [5]) have been externally added into magnesium matrix in a fibrous or particulate form as reinforcements. These various reinforcements share a number of common characteristics, including high hardness, high strength, and good thermal stability, thus significantly enhancing the material strengths at both room and high temperatures. However, ceramic materials normally have poor wettability with molten magnesium alloys and low thermal compatibility with the metal matrix. On the other hand, elemental metals such as Ni and Cu have a much greater density than that of magnesium. Use of such reinforcements not only compromises the lightweight of the final composites, but also makes it challenging to uniformly distribute these reinforcing materials in the melt. Intermetallic compounds with high thermal stability, such as nickel aluminide, are considered promising reinforcements for magnesium alloys. For instance, Al_3Ni has an elastic modulus of between 116 and 140 GPa [6, 7], density of 4.00 g/cm^3 [8], and melting point of 854°C [6], and can be an effective reinforcement for magnesium alloys. In this study, the in-situ formation behavior of nickel aluminide intermetallic

compounds in AM60B alloy is investigated, and the effects of the intermetallic compounds on tensile properties are examined.

2. Experimental methods

2.1. Sample preparation

The composition of AM60B magnesium alloy is given in Table 1. Melting was performed in a vacuum induction furnace using a plain carbon steel crucible, as schematically shown in Figure 1. Ni was added into AM60B melt in the forms of powder or wire. The powder used has a purity of 99.8% and an average particle size of 10-15 μm . The concentration of Ni powder in the alloys was aimed at 0.5 wt.% and 5 wt.%, respectively. The Ni powders were placed between two AM60B blocks in the crucible. After the AM60B block was melted, a carbon steel tubing for argon gas and thermocouple was lowered into the molten alloy, and argon gas was bubbled through the melt. The Ni wire used had a diameter of 1 mm. It was tied to the steel tubing and was lowered into the melt after the magnesium block becomes molten. Based on the mass difference of the wire before and after melting, the resulting alloy contained approximately 0.5 wt.% of nickel. The effect of argon gas agitation was studied by making two identical melting runs with and without argon gas bubbling. In all cases, the melting temperature was 700°C and the melting time was 30 minutes or 60 minutes. Following the melting, the molten alloy was poured into a steel receiving crucible kept at room temperature. After pouring, it was observed that a solid piece remained at the bottom of the melting crucible for the alloys with Ni powder addition. The size of the remaining solid piece was larger for longer melting time and the alloy with a higher

concentration of Ni addition. For comparing the effect of nickel addition, an AM60B alloy without nickel was cast into a receiving crucible after melting for 2 and 60 minutes respectively at 700°C without bubbling of argon gas. The experiments of different melting parameters and the corresponding samples are summarized in Table 2.

2.2. Material characterization and tensile tests

For microstructure characterization and composition analysis, samples were cut from the cast ingots and analyzed using an Olympus PMG3 optical microscope as well as a Hitachi S-3500 scanning electron microscope (SEM) with an energy dispersive spectrometer (EDS). Furthermore, particles in the alloy were extracted from the ingot in an ethanol solution containing 25vol.% acetic acid, and subsequently analyzed using SEM/EDS and a Philips Xpert X-ray diffractometer to examine the phase constitution.

Flat specimens cut from the cast ingots were used for tensile tests. The specimens had a total length of 100 mm and a gauge length of 25 mm. The width and thickness of the gauge length section were 6mm and 3 mm, respectively. Tensile tests were carried out using an INSTRON 8516 machine at a crosshead speed of 10 mm/min. Five specimens were tested for each melted sample.

3. Experimental results

3.1. Microstructure and phase compositions

The microstructures of the samples solidified at the bottom of the melting crucible (4-RE and 5-RE) are shown in Figure 2. The sample containing 5 wt.% of Ni (Figure 2a)

illustrates a high density of coarse particles with polygonal cross-sections and up to 10 μm in size. Figure 2b shows the microstructure of sample 4-RE. Lamellar shaped precipitates (labeled with B and C) were accompanied by a small amount of eutectic microstructure (labeled as A). The average compositions of these phases analyzed by EDS were shown in Table 3. It is clear that the particles in both samples are nickel rich, and were most likely due to the sedimentation of the heavy particles to the bottom of the crucible during melting.

The SEM micrograph of the extracted particles from samples 4-RE is illustrated in Figure 3. The cube-like shape and relatively large size of the particles indicated that these particles were formed in the liquid phase. EDS analysis revealed that the composition of the particles were 70.2Ni-22.4Al-2.3Mn-0.4Mg-4.7O in weight percentage, which is consistent with the analyzing results before extraction. X-ray diffraction pattern of the extracted particles is illustrated in Figure 4. The main phases in the extracted particles were $\text{Al}_{0.42}\text{Ni}_{0.58}$ aluminide [9] and $\text{Al}_{60}\text{Mn}_{11}\text{Ni}_4$ [10]. No peaks for elemental Ni were found, indicating that all the nickel was in the intermetallic form. Similar microstructure was found in samples 3-RE, 4-RE and 5-RE, except that the solidified mass at the bottom of the melting crucible was much greater in sample 5-RE, , showing that increase in Ni content promoted the formation of the coarse $\text{Al}_{0.42}\text{Ni}_{0.58}$ aluminide.

The effect of melting time and gas agitation on microstructure is shown in Figure 5. Longer melting time (60 minutes) along with argon gas agitation resulted in a higher

density of particles than the sample with shorter melting time (2 minutes) without argon gas agitation.

The optical micrographs of samples 1-IN, 2-IN, 6-IN and 7-IN are shown in Figure 6. The average grain size of ingot 1-IN, 2-IN, 6-IN, and 7-IN was around 400 μm , 200 μm , 200 μm , and 150 μm , respectively, corresponding to an increase in the density of the particles formed in the samples. The results showed that both longer melting time and bubbling of argon gas was beneficial to the in-situ formation of the particles and grain refinement. Figure 6 also shows that most of the particles were located within the grains.

The compositions of the matrix and particles in samples 1-IN, 2-IN, and 7-IN obtained by EDS analyses were shown in Table 4. The matrix compositions of the three samples were essentially the same, close to the nominal composition of AM60B. However, the compositions of the particles in these three samples were quite different. The particles in sample 1-IN and 2-IN contained mainly Mg, Al, Mn, and oxygen, while the particles in sample 7-IN contained a significant amount of Ni along with a minor amount of Fe, in addition to Mg, Al, Mn, and oxygen. It is unclear where the oxygen comes from. Since the melting was conducted under an argon atmosphere in a closed vacuum chamber, it was unlikely that the oxygen was picked up during melting. Considering that the samples were finish polished with 0.05 μm alumina abrasive particles, it is suspected that the oxygen present in the EDS data might be the result of surface contamination caused by embedding of fine alumina abrasive particles into the soft Mg matrix during sample preparation.

SEM/EDS analysis showed that the extracted residues from samples 1-IN and 2-IN had similar compositions and shapes. SEM image of the particles extracted from sample 2-IN are shown in Fig. 7. There were two types of particles present in the extracted residues. One was dark and large, with a size ranging from 20 μm to 50 μm . The other was bright and small, with a size around 2 μm . The SEM images also illustrate that the fine and bright particles were attached to the surface of the dark and coarse particles. EDS analysis revealed that the dark and coarse particles had a composition of 41.6wt.%Al-58.1wt.%O-0.30wt.%Mg, and the bright and fine particles had a composition of 34.3wt.%Al-59.7wt.%Mn-5.7wt.%O-0.3wt.%Mg. The EDS analysis of the two types of particles indicated that the dark and coarse particle was aluminum oxide while the bright and fine particle was a manganese aluminide. The XRD diffraction analysis of the extracted particles from sample 2-IN showed that the main constituent of the extracted residues is Al_8Mn_5 [11], as shown in Fig. 8. Aluminum oxide, however, was not detected by XRD from the residues. The most likely reason for the absence of the aluminum oxide peaks in the XRD spectrum is that the aluminum oxide is in amorphous form. Because no aluminum oxide particles were observed by SEM/EDS analysis of the bulk 1-IN and 2-IN ingots, it is believed that the coarse aluminum oxide particles were formed during the extraction process.

The extraction residue from sample 7-IN consisted of particles with a size around 5 μm , as shown in Figure 9. These fine particles had a composition of 48.3wt.%Al-23.9wt.%Mn-20.9wt.%Ni-0.9wt.%Fe-1.1wt.%Mg-4.9wt.%O. XRD pattern of the extracted particles is shown in Figure 10. The main phase in the extracted residue was

revealed to be intermetallic compound $\text{Al}_{60}\text{Mn}_{11}\text{Ni}_4$ [10]. These results confirmed that by adding nickel into the magnesium alloy during melting and properly controlling melting procedures, finely dispersed aluminide particles can be formed in the magnesium matrix.

3.2. Tensile properties

The tensile properties of the materials are shown in Figure 11. In general, increasing melting time and bubbling argon gas with Ni addition during the melting process augmented the strength and ductility of the material. The ultimate tensile strength increased from around 180 MPa for the samples without Ni addition (1-IN, 2-IN), to 236 MPa for the sample with Ni addition (7-IN). This was accompanied by significant improvement in elongation, increasing from 7% for samples without Ni addition to 12% for the sample melted with Ni and bubbling of argon gas.

The fracture surface morphologies for samples 1-IN and 7-IN are shown in Figure 12. Both samples displayed similar ductile fracture features, indicating the same fracture mechanism for these two samples.

4. Discussions

Nickel is normally considered a harmful impurity in commercial magnesium alloys, and is avoided to prevent its negative effect on corrosion resistance [12]. In the current study, nickel is intentionally added to investigate its effects on intermetallic formation behavior and on mechanical properties. The experimental results revealed that in the AM60B alloy, nickel exists primarily as the intermetallic compound $\text{Al}_{60}\text{Mn}_{11}\text{Ni}_4$ in the matrix

when the concentration of Ni is low and nickel is completely dissolved into the melt, as in the case of sample with 0.5 wt.% of nickel through dissolving fine nickel wires. When Ni was added in the powder form, a high concentration of intermetallic compound $\text{Al}_{0.42}\text{Ni}_{0.58}$ was found to co-exist with $\text{Al}_{60}\text{Mn}_{11}\text{Ni}_4$ at the bottom of the melting crucible, most likely caused by sedimentation of the nickel powder during melting. The hypothesis was supported by the fact that when Ni was added to the melt through suspended nickel wire, no $\text{Al}_{0.42}\text{Ni}_{0.58}$ aluminide particles were observed even after extended period of melting. This is because in this case nickel entered the melt in the atomic form through the dissolution of the nickel wires, and therefore minimizes sedimentation. The sedimentation of nickel powders to the bottom demonstrates the challenges commonly encountered in melting materials with ingredients having significantly different densities. The segregation also made it very difficult to accurately control and assess the nickel concentration in the bulk of the cast ingots. Clearly, the control of nickel distribution in the melt is critical for homogeneous distribution of the intermetallic compounds formed.

The formation behavior of manganese-nickel aluminide particles in the alloy depends on processing parameters, such as melting time and gas agitation. This can be understood because dissolution of Ni into the molten alloy is an essential step for the formation of Al-Mn-Ni compounds. Long melting time and gas agitation both increase promote the dissolution of nickel into the melt and hence facilitates the formation of manganese-nickel aluminide particles. In addition, gas agitation also promotes the chemical reactions between Al, Mn, and Ni.

The formation of manganese-nickel aluminide particles in the melt will result in the consumption of aluminum and lead to reduced quantity of the $\text{Mg}_{17}\text{Al}_{12}$ precipitation in the material, which is supported by XRD diffraction analysis of the bulk samples, as shown in Figure 13 and Figure 14. Clearly, the intensity of the $\text{Mg}_{17}\text{Al}_{12}$ peaks decreased when $\text{Al}_{60}\text{Mn}_{11}\text{Ni}_4$ was formed as a result of nickel addition.

Both the strength and ductility of the AM60B alloy with nickel addition increased with longer melting time and argon gas agitation. Since grain refinement is the only known strengthening mechanism that increases the strength and ductility of a material simultaneously, it can be expected that grain refinement played a key role in the observed improvement in both strength and ductility, as shown in Fig. 6. However, the fact that the strength and ductility were not steadily improved with the refinement of the grains in ingots 1-IN, 2-IN, 6-IN, and 7-IN, as shown in Figure 11, also suggests that the change of mechanical properties cannot be solely explained by grain refinement. The increased density of Al-Mn-Ni particles in the samples with longer melting time and argon gas agitation is expected to also contribute to the strengthening of the material through dispersion strengthening. However, the formation of $\text{Al}_{60}\text{Mn}_{11}\text{Ni}_4$ particles in AM60B alloy is at the cost of reduced $\text{Mg}_{17}\text{Al}_{12}$ precipitation. The net result of the increased $\text{Al}_{60}\text{Mn}_{11}\text{Ni}_4$ formation and reduced $\text{Mg}_{17}\text{Al}_{12}$ precipitation seems to increase the strength of the material. The formation of $\text{Al}_{60}\text{Mn}_{11}\text{Ni}_4$ may be particularly beneficial to high temperature strength because $\text{Al}_{60}\text{Mn}_{11}\text{Ni}_4$ is more thermally stable than $\text{Mg}_{17}\text{Al}_{12}$, judged by their melting temperature.

The many desirable characteristics of $\text{Al}_{60}\text{Mn}_{11}\text{Ni}_4$ make it a promising reinforcement phase in magnesium alloys. First, the $\text{Al}_{60}\text{Mn}_{11}\text{Ni}_4$ intermetallic particles maintained a relatively small size and homogeneous distribution in the cast ingot. This is in contrast to some other ceramic particles such as AlN [13] and intermetallic compound such as Mg_2Si [14-19] that are prone to coarsening in the magnesium melt, thus make them ineffective for dispersion strengthening. Secondly, the cost of forming in-situ $\text{Al}_{60}\text{Mn}_{11}\text{Ni}_4$ reinforcement is relatively low, as compared to the elements used in other heat resistant magnesium alloys, such as rare earth metals, silver, yttrium and strontium.

5. Conclusions

The in-situ formation behavior of the intermetallic compounds in an AM60B alloy with nickel was investigated. The following results were obtained.

- Manganese-nickel aluminide particles ($\text{Al}_{60}\text{Mn}_{11}\text{Ni}_4$) and nickel aluminide ($\text{Al}_{0.42}\text{Ni}_{0.58}$) particles can be in-situ formed in molten AM60B alloy with the addition of nickel.
- The in-situ formed manganese-nickel aluminide particles ($\text{Al}_{60}\text{Mn}_{11}\text{Ni}_4$) tend to resist coarsening in the melt and are uniformly distributed in the matrix. In contrast, nickel aluminide ($\text{Al}_{0.42}\text{Ni}_{0.58}$) particles are prone to coarsening and tend to segregate during the melting process.
- The formation behavior of the intermetallic compounds depends strongly on the Ni content in the AM60B alloy and the way in which Ni is added to the melt.
- The in-situ formed manganese-nickel aluminide particles ($\text{Al}_{60}\text{Mn}_{11}\text{Ni}_4$) refine the grains of the matrix and increase the mechanical properties of AM60B.

Acknowledgement:

The authors wish to thank Moe Islam for his valuable discussions in the course of this research work. The assistances by Bill Wells, Glen Campbell, and Mike Meinert in conducting the experiments are also gratefully acknowledged.

Reference:

- [1]. ASM specialty handbook, Magnesium and magnesium alloys, ASM International, 1999, p. 37.
- [2]. K. Wu, M. Y. Zheng, C. K. Yao, Sato, Tatsuo; Tezuka, Hiroyasu; Kamio, Akihiko; Li, D X, Journal of Materials Science Letters, Vol. 18, No. 16, 15 Aug. 1999, p. 1301-1303.
- [3]. V. Sklenicka, M. Svoboda, M. Pahutova, K. Kucharova, T.G. Langdon, Materials Science and Engineering A319–321 (2001) 741–745.
- [4]. S. F. Hassan, M. Gupta, Journal of Alloys and Compounds, Vol. 345, No. 1-2, 28 Oct. 2002, pp. 246-251.
- [5]. S. F. Hassan, K. F. Ho, and M. Gupta, Materials Letters. Vol. 58, No. 16, June 2004, pp. 2143-2146.
- [6]. D. J. Skinner, M. Zedalis, Scripta Metall., Vol. 22, 1988, pp. 1783-1785.
- [7]. Y. Fukui, K. Takashima, and C. B. Ponton, J. Mater. Sci., Vol. 29, 1994, pp. 2281-2288.
- [8]. N. Dudzinski, J. Inst. Met., Vol. 83, 1954-1955, pp. 444-448.

- [9]. JCPDS XRD diffraction card 44-1267, 1997.
- [10]. JCPDS XRD diffraction card 29-0049, 1997.
- [11]. JCPDS XRD diffraction card 18-0035, 1997
- [12]. ASM Specialty Handbook, Magnesium and Magnesium Alloys, ASM International, 1999, p.28.
- [13]. H. Z. Ye, X.Y. Liu, Journal of Materials Processing Technology, In press.
- [14]. E. E. Schmidt, K. V. Oldenburg, Z. Metallkunde, Vol. 81, P. 809, 1990.
- [15]. M. Mabuchi, K. Kubota, K. Higashi, Journal of Materials Science 31 (1996) 1529-1535.
- [16]. M. Mabuchi, T. Asahina, K. Kubota, K. Higashi, Institute of Materials (UK), PP439-447, 1997.
- [17]. M. Mabuchi, K. Kubota, K. Higashi, Materials Letter 19 (1994) 247-250.
- [18]. M. Mabuchi, K. Kubota, K. Higashi, Minerals, Metals and Materials Society/AIME (USA), PP. 463-470, 1995.
- [19]. M. Mabuchi, K. Kubota, and K. Higashi, Scripta Metallurgica et Materialia, Vol. 33, No. 2, pp. 331-335, 1995.

Table 1. The composition of AM60B alloy.

Elements	Al	Mn	Zn	Si	Cu	Fe	Ni	Mg
Content (wt.%)	5.6-6.4	0.26-0.5	<0.2	<0.05	<0.008	<0.004	<0.001	Bal.

Table 2. Different treatments for the samples.

	Treatment	Sample Designation
1	Melted for 2 min without Ni addition and without bubbling of argon	1-IN: ingot cast into the receiving crucible
2	Melted for 60 min without Ni addition and without bubbling of argon	2-IN: ingot cast into the receiving crucible
3	Melted for 60 min with 0.5wt% Ni powders added and with bubbling of argon	3-IN: ingot cast into the receiving crucible 3-RE: remainder in the melting crucible
4	Melted for 30 min with 0.5wt% Ni powders added and with bubbling of argon	4-IN: ingot cast into the receiving crucible 4-RE: remainder in the melting crucible
5	Melted for 30 min with 5.0wt% Ni powders added and with bubbling of argon	5-IN: ingot cast into the receiving crucible 5-RE: remainder in the melting crucible
6	Melted for 60 min with 0.5wt% Ni wire added and without bubbling of argon	6-IN: ingot cast into the receiving crucible
7	Melted for 60 min with 0.5wt% Ni wire added and with bubbling of argon	7-IN: ingot cast into the receiving crucible

Table 3. Compositions (wt.%) of the phases in samples 3-RE, 4-RE, and 5-RE.

Element	Mg	Al	Mn	Fe	Ni
Particles in 4-RE (Figure2a)	0.5	24.7	1.9	Undetected	72.9
Eutectic phase (A) in Figure2b.	64.4	0.7	Undetected	Undetected	34.9
Particle B in Figure2b.	0.2	20.0	0.9	0.1	78.8
Particle C in Figure2b.	26.5	4.2	0.6	0.5	68.2

Table 4. Matrix and particle compositions (wt.%) in samples 1-IN, 2-IN & 7-IN

Elements		Al	Mn	Ni	Fe	O	Mg
Sample 1-IN	Matrix	4.9	Undetected	Undetected	Undetected	2.0	Bal.
	Particle	36.7	48.0	Undetected	Undetected	3.7	Bal.
Sample 2-IN	Matrix	4.2	Undetected	Undetected	Undetected	2.8	Bal.
	Particle	21.6	20.8	Undetected	Undetected	14.6	Bal.
Sample 7-IN	Matrix	4.6	Undetected	Undetected	Undetected	2.1	Bal.
	Particle	21.7	14.6	10.5	0.7	9.9	Bal.

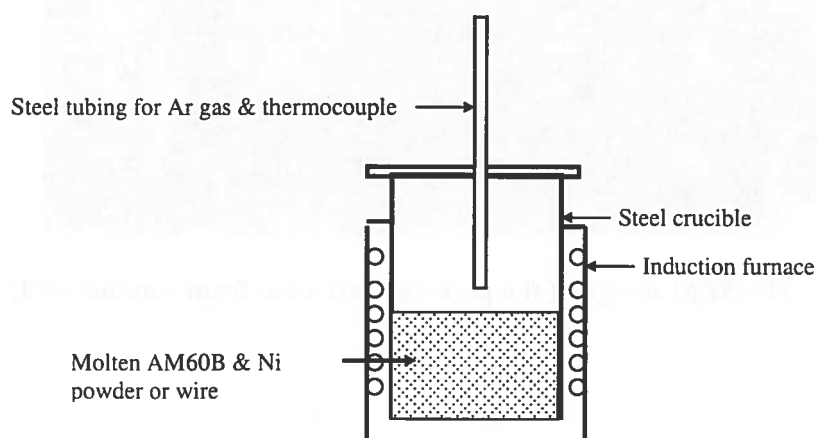
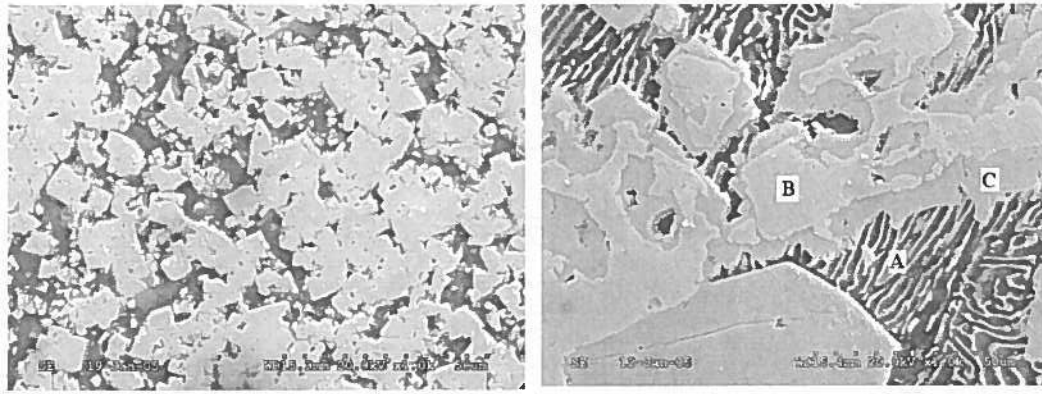


Figure 1. Schematic illustration of the melting setup.



(a)

(b)

Figure 2. SEM microstructures of the solid piece remaining in the melting crucible

(a) Sample 5-RE (5 wt.% Ni), (b) Sample 4-RE (0.5 wt.% Ni)

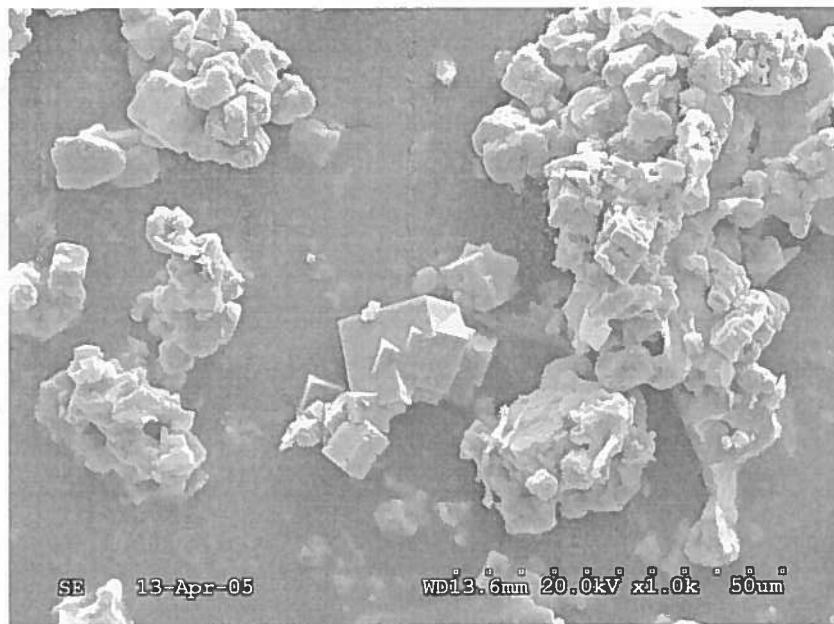


Figure 3. The SEM image of the particles extracted from sample 4-RE.

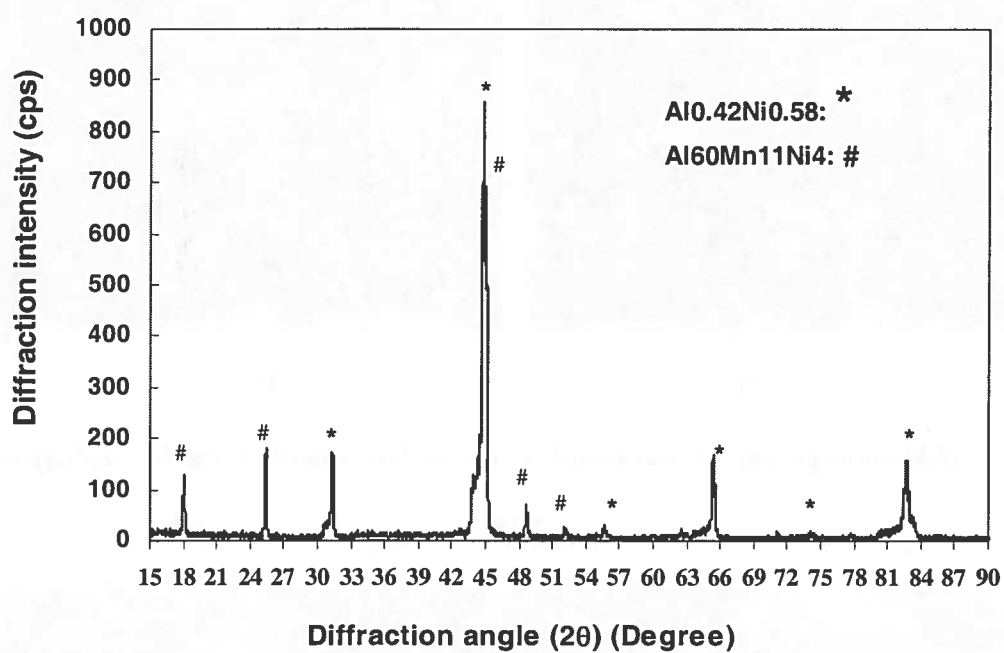
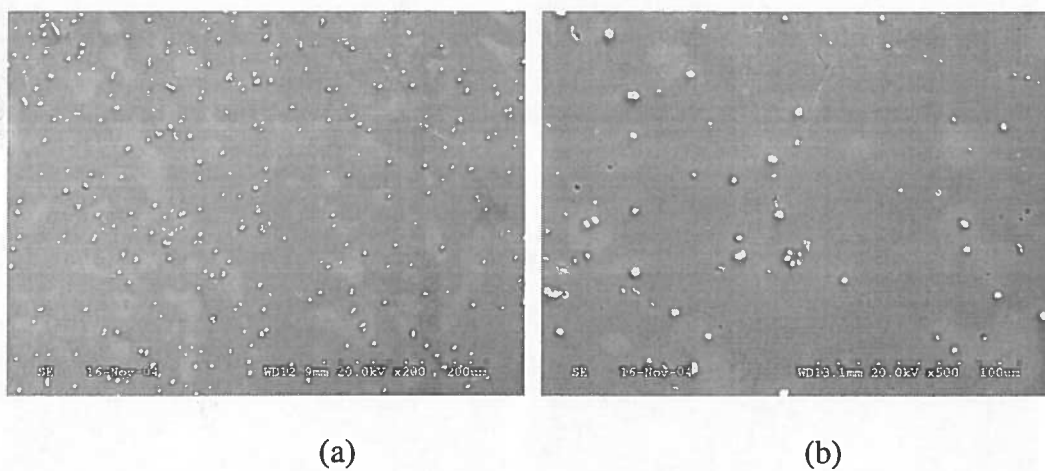
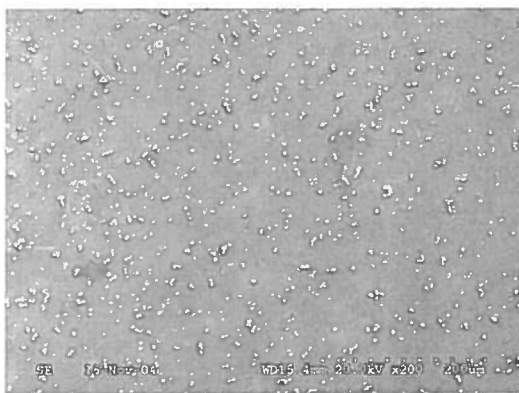
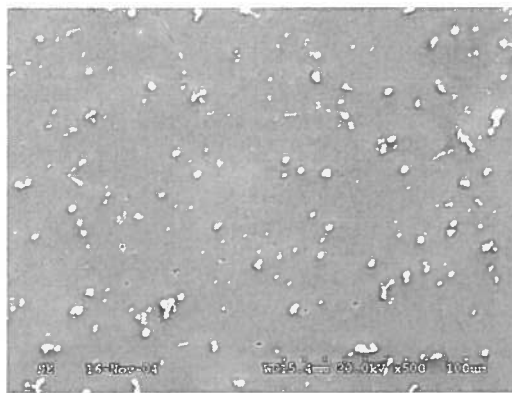


Figure 4. The (Cu-K α) XRD pattern of the extracted particles from sample 4-RE.



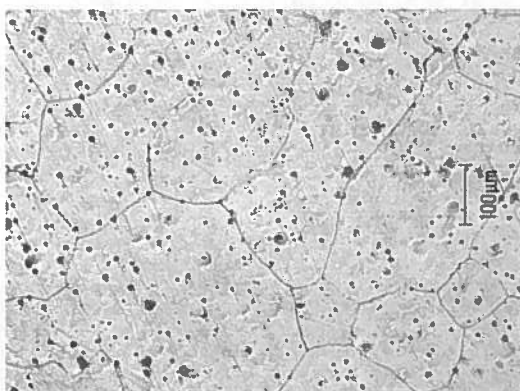


(c)

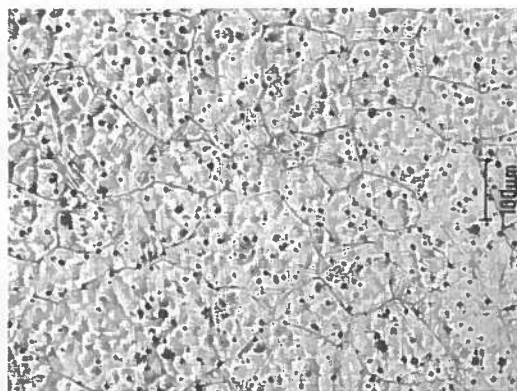


(d)

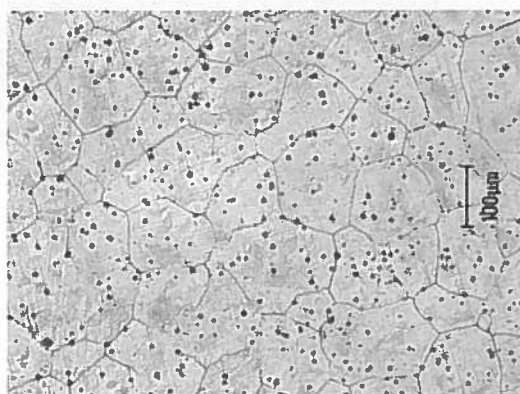
Figure 5. SEM micrographs of cast samples: (a) and (b) sample 1-IN; (c) and (d) sample 7-IN.



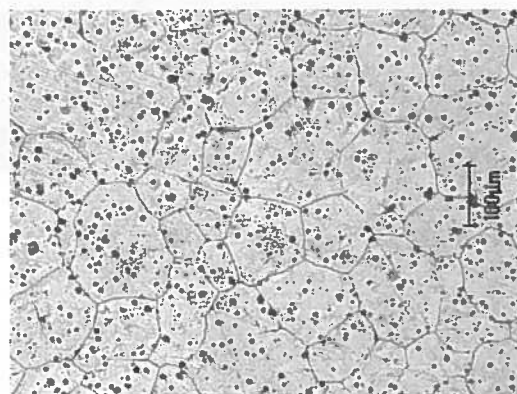
(a)



(b)



(c)



(d)

Figure 6. The optical images of the cast ingot: (a) sample 1-IN; (b) sample 2-IN, (c) sample 6-IN, and (d). sample 7-IN.

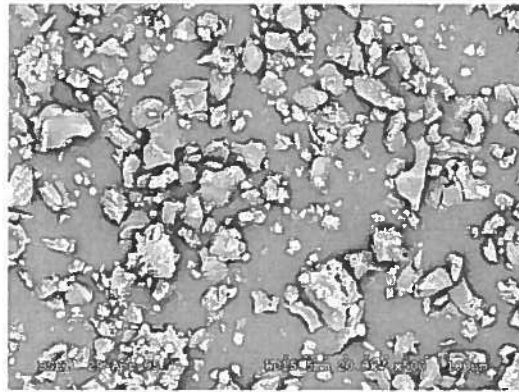


Fig. 7. SEM images of the extracted particles from sample 2-IN.

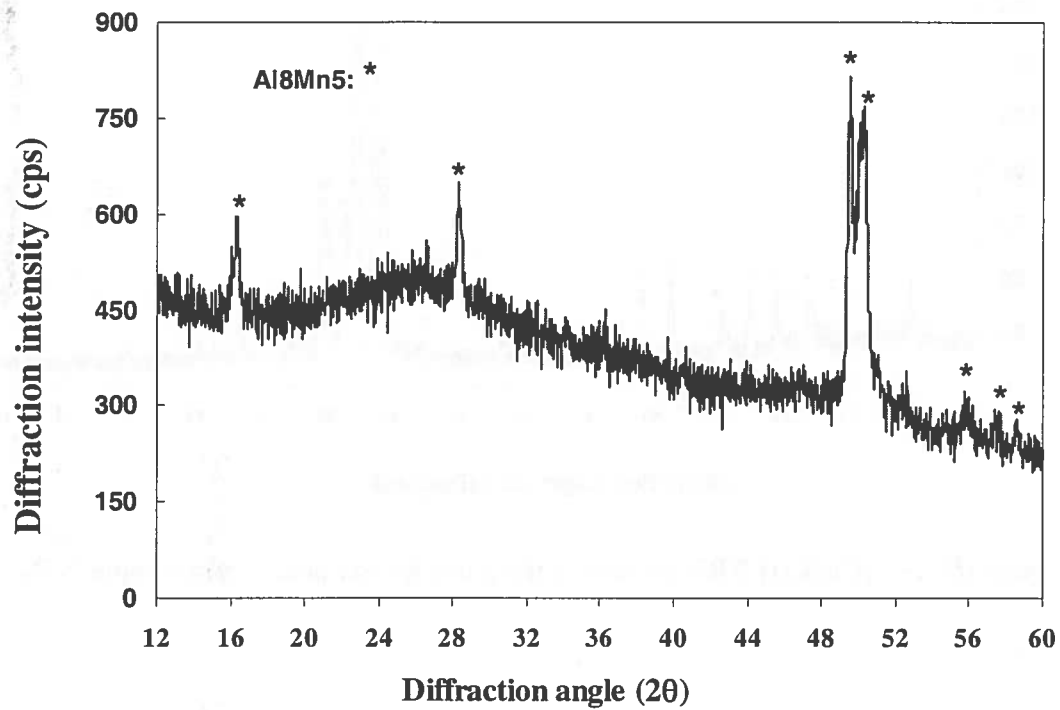


Fig. 8. (Co-K α) XRD pattern for the particles extracted from 2-IN ingot.

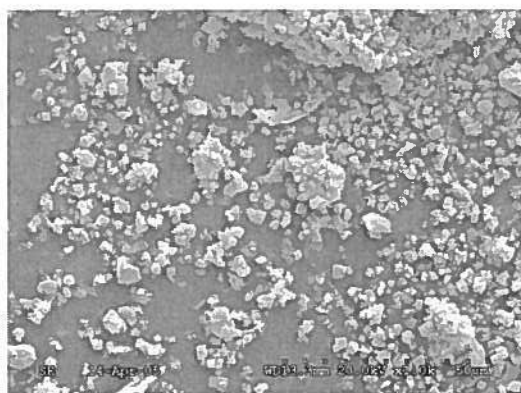


Figure 9. SEM image of particles extracted from sample 7-IN.

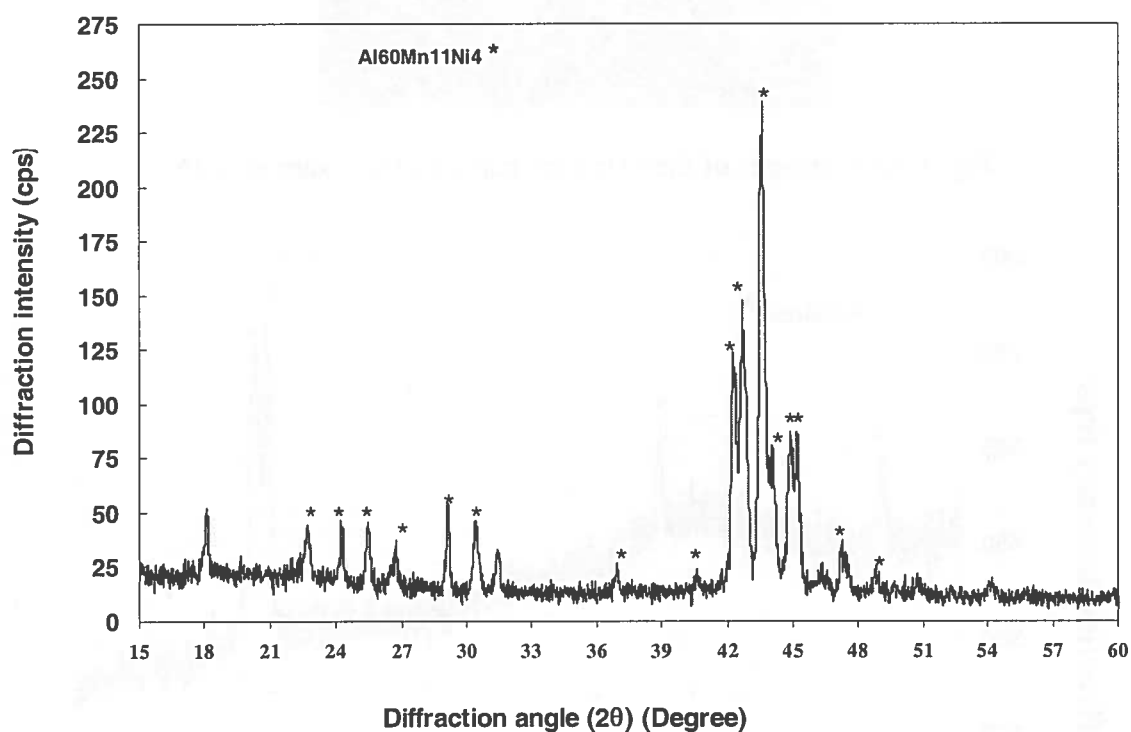


Figure 10. The (Cu-K α) XRD pattern of the particles extracted from sample 7-IN.

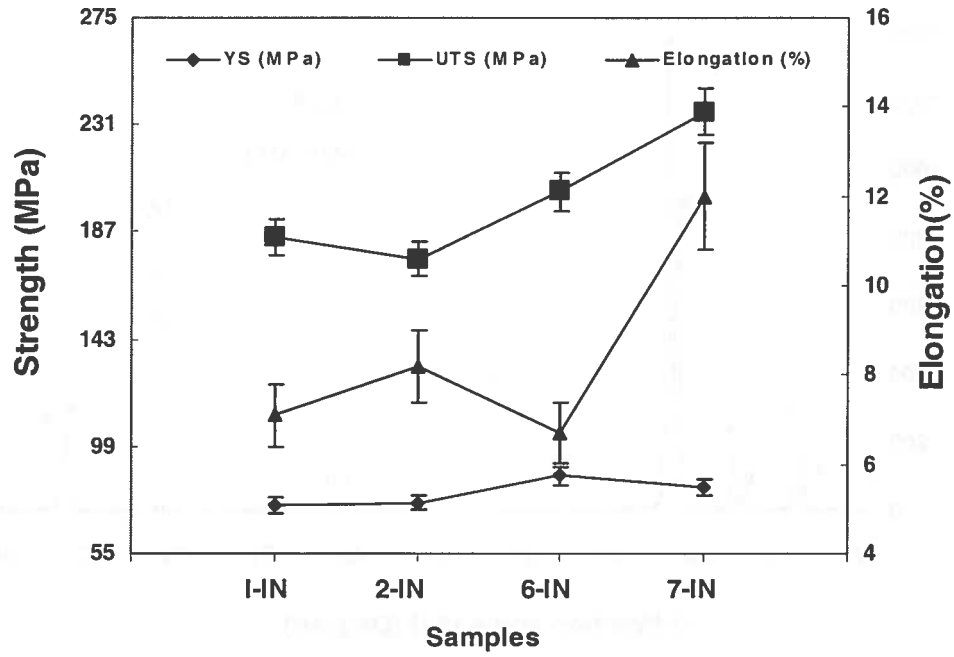
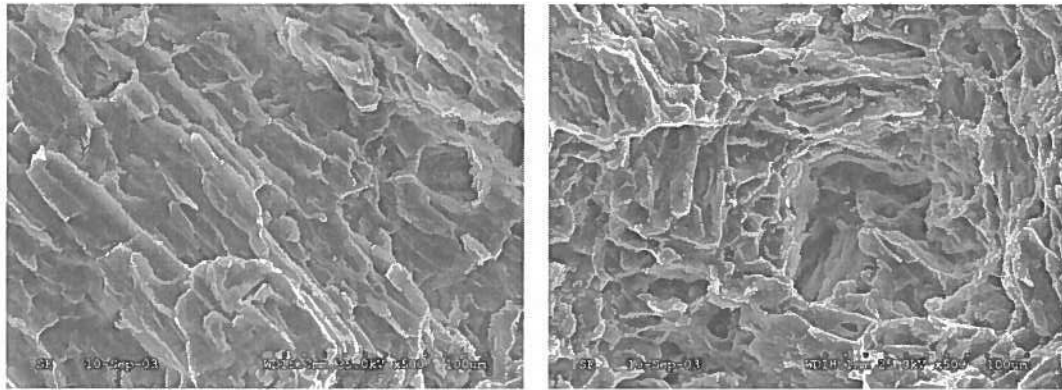


Figure 11. The tensile performance of the differently processed ingots.



(a)

(b)

Figure 12. Fracture surface morphology of samples 1-IN (a) and 7-IN (b).

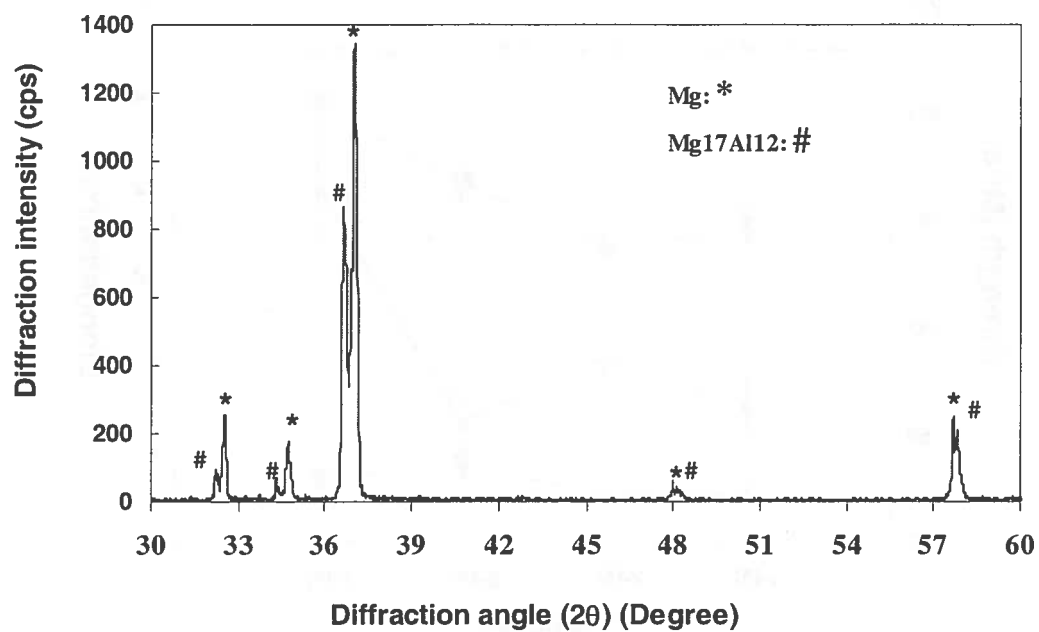


Figure 13. The (Cu-K α) XRD pattern of ingot 1-IN.

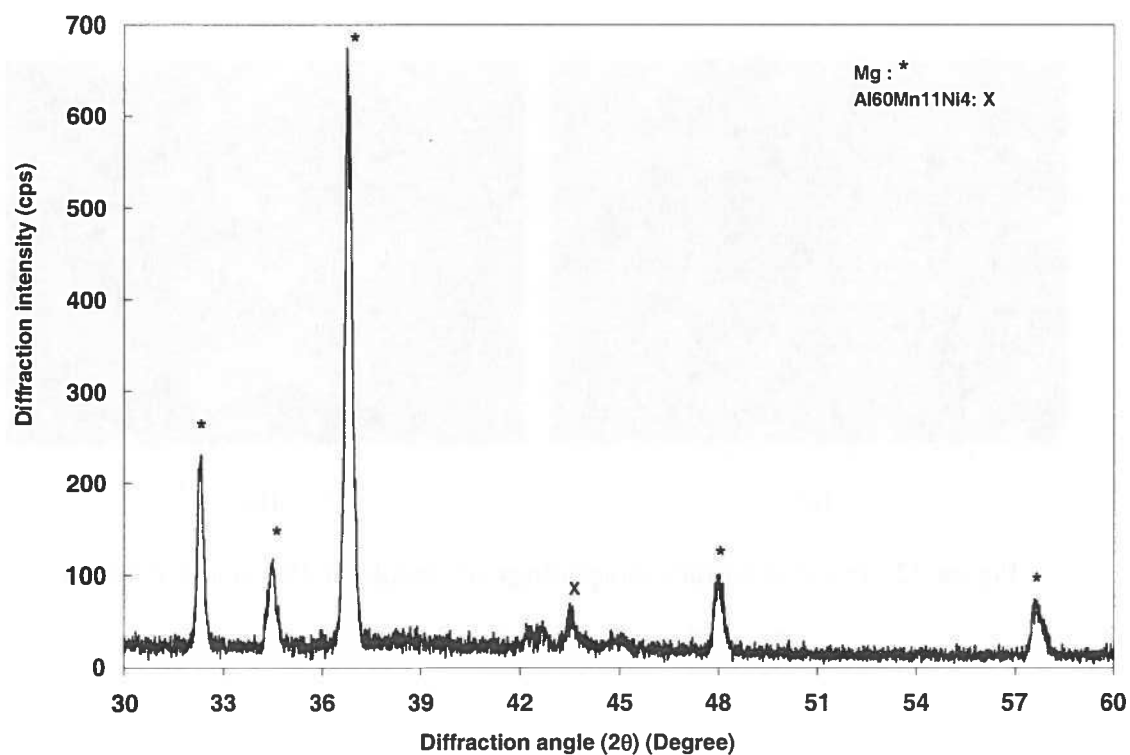


Figure 14. The (Cu-K α) XRD pattern of ingot 7-IN.

Table and figure captions

Table 1. The composition of AM60B alloy.

Table 2. Different treatments for the samples.

Table 3. Compositions (wt.%) of the phases in samples 3-RE, 4-RE, and 5-RE.

Table 4. Matrix and particle compositions (wt.%) in samples 1-IN, 2-IN & 7-IN

Figure 1. Schematic illustration of the melting setup.

Figure 2. SEM microstructures of the solid piece remaining in the melting crucible

Sample 5-RE (5 wt.% Ni), (b) Sample 4-RE (0.5 wt.% Ni)

Figure 3. The SEM image of the particles extracted from sample 4-RE.

Figure 4. The (Cu-K α) XRD pattern of the extracted particles from sample 4-RE.

Figure 5. SEM micrographs of cast samples: (a) and (b) sample 1-IN; (c) and (d) sample 7-IN.

Figure 6. The optical images of the cast ingot: (a) sample 1-IN; (b) sample 2-IN, (c) sample 6-IN, and (d). sample 7-IN.

Fig. 7. SEM images of the extracted particles from sample 2-IN.

Fig. 8. (Co-K α) XRD pattern for the particles extracted from 2-IN ingot.

Figure 9. SEM image of particles extracted from sample 7-IN.

Figure 10. The (Cu-K α) XRD pattern of the particles extracted from sample 7-IN.

Figure 11. The tensile performance of the differently processed ingots.

Figure 12. Fracture surface morphology of samples 1-IN (a) and 7-IN (b).

Figure 13. The (Cu-K α) XRD pattern of ingot 1-IN.

Figure 14. The (Cu-K α) XRD pattern of ingot 7-IN.

1975-1976 Long-Term

The following table shows the results of the 1975-1976 Long-Term study. The data is presented in a table format, with the first column representing the year and the subsequent columns representing the different categories of the study. The data is presented in a table format, with the first column representing the year and the subsequent columns representing the different categories of the study. The data is presented in a table format, with the first column representing the year and the subsequent columns representing the different categories of the study.

Year	Category 1	Category 2	Category 3	Category 4	Category 5
1975	100	200	300	400	500
1976	150	250	350	450	550
1977	200	300	400	500	600
1978	250	350	450	550	650
1979	300	400	500	600	700
1980	350	450	550	650	750
1981	400	500	600	700	800
1982	450	550	650	750	850
1983	500	600	700	800	900
1984	550	650	750	850	950
1985	600	700	800	900	1000
1986	650	750	850	950	1050
1987	700	800	900	1000	1100
1988	750	850	950	1050	1150
1989	800	900	1000	1100	1200
1990	850	950	1050	1150	1250
1991	900	1000	1100	1200	1300
1992	950	1050	1150	1250	1350
1993	1000	1100	1200	1300	1400
1994	1050	1150	1250	1350	1450
1995	1100	1200	1300	1400	1500
1996	1150	1250	1350	1450	1550
1997	1200	1300	1400	1500	1600
1998	1250	1350	1450	1550	1650
1999	1300	1400	1500	1600	1700
2000	1350	1450	1550	1650	1750
2001	1400	1500	1600	1700	1800
2002	1450	1550	1650	1750	1850
2003	1500	1600	1700	1800	1900
2004	1550	1650	1750	1850	1950
2005	1600	1700	1800	1900	2000
2006	1650	1750	1850	1950	2050
2007	1700	1800	1900	2000	2100
2008	1750	1850	1950	2050	2150
2009	1800	1900	2000	2100	2200
2010	1850	1950	2050	2150	2250
2011	1900	2000	2100	2200	2300
2012	1950	2050	2150	2250	2350
2013	2000	2100	2200	2300	2400
2014	2050	2150	2250	2350	2450
2015	2100	2200	2300	2400	2500
2016	2150	2250	2350	2450	2550
2017	2200	2300	2400	2500	2600
2018	2250	2350	2450	2550	2650
2019	2300	2400	2500	2600	2700
2020	2350	2450	2550	2650	2750
2021	2400	2500	2600	2700	2800
2022	2450	2550	2650	2750	2850
2023	2500	2600	2700	2800	2900
2024	2550	2650	2750	2850	2950
2025	2600	2700	2800	2900	3000
2026	2650	2750	2850	2950	3050
2027	2700	2800	2900	3000	3100
2028	2750	2850	2950	3050	3150
2029	2800	2900	3000	3100	3200
2030	2850	2950	3050	3150	3250
2031	2900	3000	3100	3200	3300
2032	2950	3050	3150	3250	3350
2033	3000	3100	3200	3300	3400
2034	3050	3150	3250	3350	3450
2035	3100	3200	3300	3400	3500
2036	3150	3250	3350	3450	3550
2037	3200	3300	3400	3500	3600
2038	3250	3350	3450	3550	3650
2039	3300	3400	3500	3600	3700
2040	3350	3450	3550	3650	3750
2041	3400	3500	3600	3700	3800
2042	3450	3550	3650	3750	3850
2043	3500	3600	3700	3800	3900
2044	3550	3650	3750	3850	3950
2045	3600	3700	3800	3900	4000
2046	3650	3750	3850	3950	4050
2047	3700	3800	3900	4000	4100
2048	3750	3850	3950	4050	4150
2049	3800	3900	4000	4100	4200
2050	3850	3950	4050	4150	4250
2051	3900	4000	4100	4200	4300
2052	3950	4050	4150	4250	4350
2053	4000	4100	4200	4300	4400
2054	4050	4150	4250	4350	4450
2055	4100	4200	4300	4400	4500
2056	4150	4250	4350	4450	4550
2057	4200	4300	4400	4500	4600
2058	4250	4350	4450	4550	4650
2059	4300	4400	4500	4600	4700
2060	4350	4450	4550	4650	4750
2061	4400	4500	4600	4700	4800
2062	4450	4550	4650	4750	4850
2063	4500	4600	4700	4800	4900
2064	4550	4650	4750	4850	4950
2065	4600	4700	4800	4900	5000
2066	4650	4750	4850	4950	5050
2067	4700	4800	4900	5000	5100
2068	4750	4850	4950	5050	5150
2069	4800	4900	5000	5100	5200
2070	4850	4950	5050	5150	5250
2071	4900	5000	5100	5200	5300
2072	4950	5050	5150	5250	5350
2073	5000	5100	5200	5300	5400
2074	5050	5150	5250	5350	5450
2075	5100	5200	5300	5400	5500
2076	5150	5250	5350	5450	5550
2077	5200	5300	5400	5500	5600
2078	5250	5350	5450	5550	5650
2079	5300	5400	5500	5600	5700
2080	5350	5450	5550	5650	5750
2081	5400	5500	5600	5700	5800
2082	5450	5550	5650	5750	5850
2083	5500	5600	5700	5800	5900
2084	5550	5650	5750	5850	5950
2085	5600	5700	5800	5900	6000
2086	5650	5750	5850	5950	6050
2087	5700	5800	5900	6000	6100
2088	5750	5850	5950	6050	6150
2089	5800	5900	6000	6100	6200
2090	5850	5950	6050	6150	6250
2091	5900	6000	6100	6200	6300
2092	5950	6050	6150	6250	6350
2093	6000	6100	6200	6300	6400
2094	6050	6150	6250	6350	6450
2095	6100	6200	6300	6400	6500
2096	6150	6250	6350	6450	6550
2097	6200	6300	6400	6500	6600
2098	6250	6350	6450	6550	6650
2099	6300	6400	6500	6600	6700
2100	6350	6450	6550	6650	6750